Applied Water Science (2026) 16:162
https://doi.org/10.1007/s13201-026-02842-w

ORIGINAL ARTICLE

Simple synthesis of $NiMn_2O_4$/$CuMn_2O_4$/chitosan nanocomposites as a novel adsorbent for methyl orange removal from water and investigation of adsorption kinetics and isotherm models

Malihe Samadi Kazemi[1] · Zeinab Izanloo[2] · Azam Sobhani[2]

Received: 28 February 2025 / Accepted: 9 April 2026 / Published online: 29 April 2026
© The Author(s) 2026

Abstract
The main objective of this research is to develop an efficient nanocomposite adsorbent for the rapid removal of organic pollutants from aqueous media. For this purpose, $NiMn_2O_4$ nanostructures (NMO) and $NiMn_2O_4$/$CuMn_2O_4$/chitosan nanocomposites (Ni/Cu/CS) were synthesized using Allium cepa (onion extract) and applied, for the first time, to remove methyl orange (MO) dye. The synthesized materials were characterized. Using response surface methodology (RSM), optimum adsorption conditions were pH = 3, adsorbent dose = 1.2 g/L, MO concentration = 10 mg/L, contact time = 5 min, and agitation speed = 300 rpm. Adsorption followed the Langmuir model (maximum capacity = 416.67 mg/g, KL = 0.01) and pseudo-second-order kinetics (R^2 = 0.9964). The outstanding and ultra-fast adsorption of Ni/Cu/CS highlights its strong potential for wastewater treatment applications.

Keywords Chemical synthesis · Nickel manganese oxide · Chitosan · Nanocomposite · Isotherm model · Adsorption kinetics

Introduction

Water pollution seriously affects human health due to the presence of toxic pollutants and the wastewater discharge (including urban and industrial wastewater) (Beshkar et al. 2022; Krishna et al. 2019; Losetty et al. 2024; Mousavi-Kamazani 2019; Rahmatolahzadeh et al. 2017; Zinatloo-Ajabshir et al. 2020a, b). Wastewater containing dyes is discharged from many industries, including cosmetics, textiles, paper, agriculture, wood, plastic, and leather. This creates serious environmental problems (Etana et al. 2025). Among them, the textile industry is the largest consumer of dyes and produces a high volume of wastewater with significant dye concentrations (10–100 mg/L) (Ahmad and Alrozi 2011). The research shows that 15–20% of the dye materials used in these industries enter the sewage (Lakkaboyana et al. 2021). Dyes have aromatic structures and can absorb light (at $350 < \lambda < 700$ nm) (Zinatloo-Ajabshir et al. 2019). The discharge of dye-containing wastewater into aquatic ecosystems damages natural landscapes (Bayat et al. 2018; Mohassel et al. 2018; Zhang et al. 2013; Zinatloo-Ajabshir, Morassaei, Amiri, Salavati-Niasari, et al., 2020). Mostly dye materials have one or more benzene rings, which can cause irreparable damage due to their toxicity. MO anionic dye is in the category of azo dyes, which is used in textile, food, printing, and pharmaceutical sectors. MO can cause problems for human health and the environment because of the having −N=N− bonds and low biodegradability. This dye is very toxic and resistant to light and washing, and does not decompose easily. The role of dyes in industrial wastewater is significant, and their degradation rate is low. We are interested in destroying dyes because of their adverse effect on human life. Removing toxin dyes from the environment and water is an urgent need. Most dyes used in industries do not degrade because they create strong complexes.

Communicated by Saad A. Aljlil

✉ Azam Sobhani
sobhani@kub.ac.ir

[1] Department of Chemistry, Boj.C., Islamic Azad University, Bojnord, Iran

[2] Department of Chemistry, Kosar University of Bojnord, Bojnord 94531–55168, Islamic Republic of Iran

Methods such as ion exchange, membrane filters, coagulation and flocculation, and oxidation, which are common wastewater treatments, are unsuitable for dye removal (Fayad et al. 2025). On the other hand, these methods produce significant amounts of sludge (Madrakian et al. 2013; Thamer et al. 2023). The surface adsorption process is one of the methods used in treatment, mainly when activated carbon is used as the adsorbent (Guo et al. 2025).

Activated carbon has been widely used to remove organic pollutants due to its high adsorption capacity, favorable physical properties, and high efficiency (Carreño Hernández et al. 2025). However, its application faces limitations due to certain drawbacks, such as the difficulty in separating powdered activated carbon, challenges in regeneration, and high costs (Chen et al. 2025). Recently, nanocomposites have been widely studied for wastewater treatment applications (Amini et al. 2021; Ghiyasiyan-Arani et al. 2017; Karimi Anjiraki et al. 2024; Monsef et al. 2021; Zinatloo-Ajabshir and Salavati-Niasari 2019). Among these, manganese-based ternary metal oxides have attracted significant research interest (Sharma and Sharma 2020). Various types of spinel metal oxides and their nanocomposites have been reported in the literature (Chani et al. 2019). These spinel metal oxide nanocomposites exhibit unique properties that make them effective adsorbents for dye removal.

The quaternized magnetic chitosan exhibited a very high adsorption capacity for methyl orange (486.13 mg/g) under optimized conditions, confirming the key role of chitosan in enhancing adsorption performance (Wang et al. 2025). In addition, MnO_2/chitosan nanocomposites were reported to effectively remove Cr(VI) from water, with adsorption driven mainly by electrostatic interactions and well described by the Sips isotherm (Dinh et al. 2020). Cross-linked chitosan/$MnFe_2O_4$ nanocomposites have also been developed for U(VI) and Th(IV) adsorption, achieving high capacities and rapid kinetics (Alaqarbeh et al. 2023). In this study, leveraging the unique properties of $NiMn_2O_4$, $CuMn_2O_4$, and chitosan, we developed an effective strategy to enhance the adsorption capabilities of spinel metal oxides through their combination with chitosan for MO removal. The surface properties of the complexes can be modified and enhanced through functionalization with chitosan. Chitosan is a non-toxic biopolymer with selective adsorption ability. Its unique structure and biological properties make it effective for removing pollutants from water (Sobhani 2022, 2024). In this study, we report for the first time the successful preparation of Ni/Cu/CS nanocomposites. The reasons for choosing this topic are environmental concerns, the demand for green synthesis, and the design of new materials with high absorption performance. The development of nanocomposites through green and low-toxicity methods remains a challenge. In this work, the use of Allium cepa extract helps to solve this challenge. Many adsorbents reported in the literature suffer from slow kinetics and moderate adsorption capacity. Achieving high capacity and ultra-fast adsorption is a critical challenge. Adsorption performance is sensitive to operating conditions (pH, adsorbent dosage, and pollutant concentration). Identifying the optimal parameters through systematic design is essential but challenging. Translating the results from batch laboratory conditions to real wastewater treatment scenarios remains an open challenge and requires further evaluation of recyclability and long-term stability. The novelty of this work lies in the development and synthesis of a novel chitosan-based nanocomposite material. Recent years have seen growing interest in environmentally benign synthesis approaches, owing to their inherent safety, natural abundance, and operational simplicity. In this study, we report the novel application of Allium cepa as a green capping agent for the synthesis of spinel nickel oxide nanocomposites. This facile and scalable methodology demonstrates significant potential for extension to other spinel-type metal oxide systems.

This work is the first comprehensive study on the adsorption mechanism and removal efficiency of Ni/Cu/CS nanocomposites for MO elimination. Detailed kinetic and isotherm analyses were performed. RSM was applied to optimize the experimental design, allowing model development, process optimization, and variance analysis with fewer experiments. The adsorption capacity of the Ni/Cu/CS nanocomposites was evaluated using four well-established isotherm models: Langmuir (Zhang et al. 2021), Freundlich (Ahmadipouya et al. 2021), Temkin (Feng et al. 2021), and Dubinin-Radushkevich (Ahmad and Ansari 2021). The adsorption kinetics were examined using pseudo-first-order, pseudo-second-order, Elovich, and intraparticle diffusion models. These analyses clarified the mechanisms and identified key kinetic parameters.

Experimental

Materials and characterization

We purchased Mn $(NO_3)_2.4H_2O$, Ni $(NO_3)_2.6H_2O$, Cu $(NO_3)_2.3H_2O$, NH_3 solution (25%), chitosan, MO, sucrose, and ethanol from Merck. We applied a Philips X′pertPro diffractometer with Ni-filtered Cu Kα radiation (λ = 1.54 Å) to investigate XRD patterns (X-ray diffraction) and a Tescan Mira3 FE-SEM microscope (Scanning Electron Microscope) to identify the morphology and the percentage of the elements in the samples. Also, a Philips EM208 TEM microscope (Transmission Electron Microscope) with 200 kV accelerating voltage was used to determine the morphology accurately. The Evolution 300 and Nicolet IS 10

Table 1 The different conditions for the synthesis of NMO and Ni/Cu/CS adsorbents are discussed in this work

Sample	Precursors	Capping agent	Synthesis method	pH	T and t of hydrothermal	Product
1	$Ni(NO_3)_2.6H_2O + Mn(NO_3)_2.4H_2O$	Sucrose	Hydrothermal	9	180 ˚C, 12 h	$NiMn_2O_4$/NiO
2	$Ni(NO_3)_2.6H_2O + Mn(NO_3)_2.4H_2O$	Allium cepa	Hydrothermal	9	180 ˚C, 12 h	$NiMn_2O_4$ Nanorods (diameter = 200–600 nm) Nanoparticles (diameter < 50 nm)
3	$Cu(NO_3)_2.3H_2O + Mn(NO_3)_2.4H_2O$	Allium cepa	Hydrothermal	9	180 ˚C, 12 h	$CuMn_2O_4$ [8]
4	$Ni(NO_3)_2.6H_2O + Cu(NO_3)_2.3H_2O + Mn(NO_3)_2.4H_2O$	Sucrose	Hydrothermal	9	180 ˚C, 12 h	$Cu + CuO + Cu_2O$
5	sample 2 + sample 3 + chitosan (1:1:2)	–	Stirring for 24 h at RT	–	–	Ni/Cu/CS nanocomposites Agglomerated nanorods/nanostructures with irregular shapes
6	sample 2 + sample 3 + chitosan (2:1:3)	–	Stirring for 24 h at RT	–	–	Ni/Cu/CS nanocomposites Agglomerated nanorods/nanostructures with irregular shapes

T Temperature, *t* Time, *h* Hour, *RT* Room temperature

Table 2 The factor levels in the RSM-CCD model

Factor	Symbol	Units	Low	High	Level
Time	A	min	3.00	60.00	3, 30, 60
Adsorbent dose	B	gr/L	0.1000	1.0000	0.1, 0.55, 1
pH	C	–	2.00	9.00	2, 5.5, 9
Agitation speed	D	rpm	100.00	500.00	100, 300, 500
Initial concentration	E	mg/L	0.1000	10.00	0.1, 5, 10

spectrophotometers from the Thermo Scientific American company were applied to study UV-Vis (UV-vis spectroscopy) and FT-IR (Fourier-transform infrared spectroscopy) spectra, respectively. A Meghnatis Kavir Kashan Co VSM (Vibrating sample magnetometer) from Kashan of Iran was used to study the magnetic properties of the photocatalysts.

Synthesis of $NiMn_2O_4$

$NiMn_2O_4$ was prepared by using a simple hydrothermal method. Usually, this method will have reasonable control over the phase formation and composition of the products (Sobhani and Salavati-Niasari 2015). Ni $(NO_3)_2.6H_2O$ and Mn $(NO_3)_2.4H_2O$ were taken in a 1:2 ratio, as precursors. The Mn $(NO_3)_2.4H_2O$ solution was added to the $Ni(NO_3)_2.6H_2O$ solution. Then allium cepa (capping agent) was added and the obtained solution stirred for 15 min. Sucrose was also used to investigate the effect of the capping agent as shown in Table 1. In the next step, NH_3 was added to adjust the pH (pH = 9). Then, the obtained solution was transferred into a stainless steel Teflon-lined autoclave. It was maintained at 180 ˚C for 12 h, and the obtained products were washed with water and ethanol and then dried at 60 ˚C. The final residue was annealed in a furnace at 850 ˚C for two h.

Synthesis of $CuMn_2O_4$

The procedure and the synthesis conditions for $CuMn_2O_4$ (CMO, sample 3) have been described in the author's published paper in detail (Samadi Kazemi and Sobhani 2023).

Synthesis of $NiMn_2O_4$/$CuMn_2O_4$/chitosan nanocomposites as adsorbent

$NiMn_2O_4$/$CuMn_2O_4$/chitosan nanocomposites were synthesized with 1:1:1 weight ratio of $NiMn_2O_4$, $CuMn_2O_4$ and chitosan. For the adsorbent preparation, first the chitosan was dissolved in acetic acid and distilled water, with a 1:10 ratio. Then $NiMn_2O_4$ prepared in this work (sample 2) and $CuMn_2O_4$ prepared in our previous work (sample 3) were added into chitosan solution. After 24 h of stirring, the adsorbent was washed with water and ethanol. Then it was dried at 60 ˚C for four h. The different experiments for synthesizing the adsorbent have been summarized in Table 1.

Adsorption experiments using the CCD model

We accomplished the response surface methodology of central composite design (RSM − CCD) to optimize the MO adsorption onto the prepared adsorbent. Hence, pH, adsorbent dosage, MO concentration, contact time, and agitation speed were investigated as the independent variables at three levels (−1, 0, +1), and the removal efficiency of MO was considered as the response factor. The levels of the three independent variables have been represented in Table 2. In this research, we used Design-Expert software for data analysis. The software version was 13, Stat-ease, Inc., Minneapolis, MN, USA.

Kinetic adsorption experiments

We used adsorption kinetic models to determine the adsorption rate and predict the process over time. The experiments were done in 8 beakers to investigate the effect of contact time on the MO removal from aqueous media. 1.2 g/L of adsorbent (Ni/Cu/CS) and 50 mL of the MO solution (concentration = 10 mg/L) were added to the beakers and pH at 3 was adjusted. The solutions were stirred for 1 to 20 min. Then, by centrifuging, the Ni/Cu/CS was separated from the solution (4000 rpm for 5 min), and the residual concentration of MO in the solution was measured. The measurements were done using a UV–Vis spectroscopy at λmax = 464 nm.

Adsorption isotherm experiments

To determine the adsorption isotherm, 50 mL of MO solution (10 mg/L) was mixed with 1.2 g/L of adsorbent at pH 3. The mixture was stirred at 300 rpm for 5 min using a shaker. The adsorption isotherm parameters of MO solution with adsorbent were calculated for different models. All tests were performed at ambient temperature. The results are written in Table 3.

Result and discussion

XRD patterns

XRD technique was used for tracking the crystal structure, phase and purity of the samples. Figure 1 shows XRD patterns of the products prepared via the hydrothermal method, in the presence of different capping agents, after calcination at 850 ˚C for two h. Figure 1a and b indicate the XRD patterns of the products prepared from Ni and Mn salts with sucrose (sample 1) and allium cepa (sample 2). The products are crystalline and composed of $NiMn_2O_4$ and NiO for sample 1, as shown in Fig. 1a. The peaks at 18.49˚, 30.34˚, 35.75˚, 37.31˚, 43.35˚, 53.87˚, 57.45˚, and 62.92˚ are in agreement with the cubic phase of $NiMn_2O_4$ (JCPDS No. 01–074-1865) and correspond to diffractions from the (111), (220), (311), (222), (400), (422), (511) and (440) planes, respectively. The peaks of $NiMn_2O_4$ have been indexed with blue color in Fig. 1. Also, peaks at 37.31˚, 43.35˚, and 62.92˚ exhibit the formation of cubic NiO with JCPDS No. 01–075-0197. Three characteristic peaks of NiO have been marked with red color by their indices ((111), (200), and (220)) in Fig. 1a. All of the peaks in the diffraction pattern of Fig. 1b have been labeled. This figure shows the product

Table 3 The parameters of the adsorption isotherms for MO adsorption on Ni/Cu/CS

Model	Parameter	Value
Langmuir; $\frac{1}{q_e} = \frac{1}{q_m K_L C_e} + \frac{1}{q_m}$		
	$q_{max}\left(mg\ g^{-1}\right)$	416.67
	$K_L\left(L\ mg^{-1}\right)$	0.01
	R^2	0.9999
Freundlich; $Ln\ q_e = LnK_f + \frac{1}{n_f} LnC_e$		
	$K_f\left(L\ mg^{-1}\right)$	3.46
	n_f	4.12
	R^2	0.8407
Temkin; $q_e = \beta\ LnK_T + \beta\ LnC_e$		
	$K_T\left(L\ mg^{-1}\right)$	118.09
	β	0.7864
	R^2	0.8909
Dubinin-Radushkevich; $Lnq_e = Lnq_s - K\left(RTLn\left(1 + \frac{1}{C_e}\right)^2\right)$		
	$q_s\left(mg\ g^{-1}\right)$	125.34
	k	3.03
	R^2	0.9695

q_m Maximum adsorption capacity, K_L Langmuir equilibrium constant, n_f *and* K_f Freundlich constants, β Temkin constant, K_T Maximum energy band, ε Polanyi potential, q_s Theoretical capacity at saturation state, T Absolute temperature, R Universal gas constant (8.314 J mol^{-1} K^{-1})

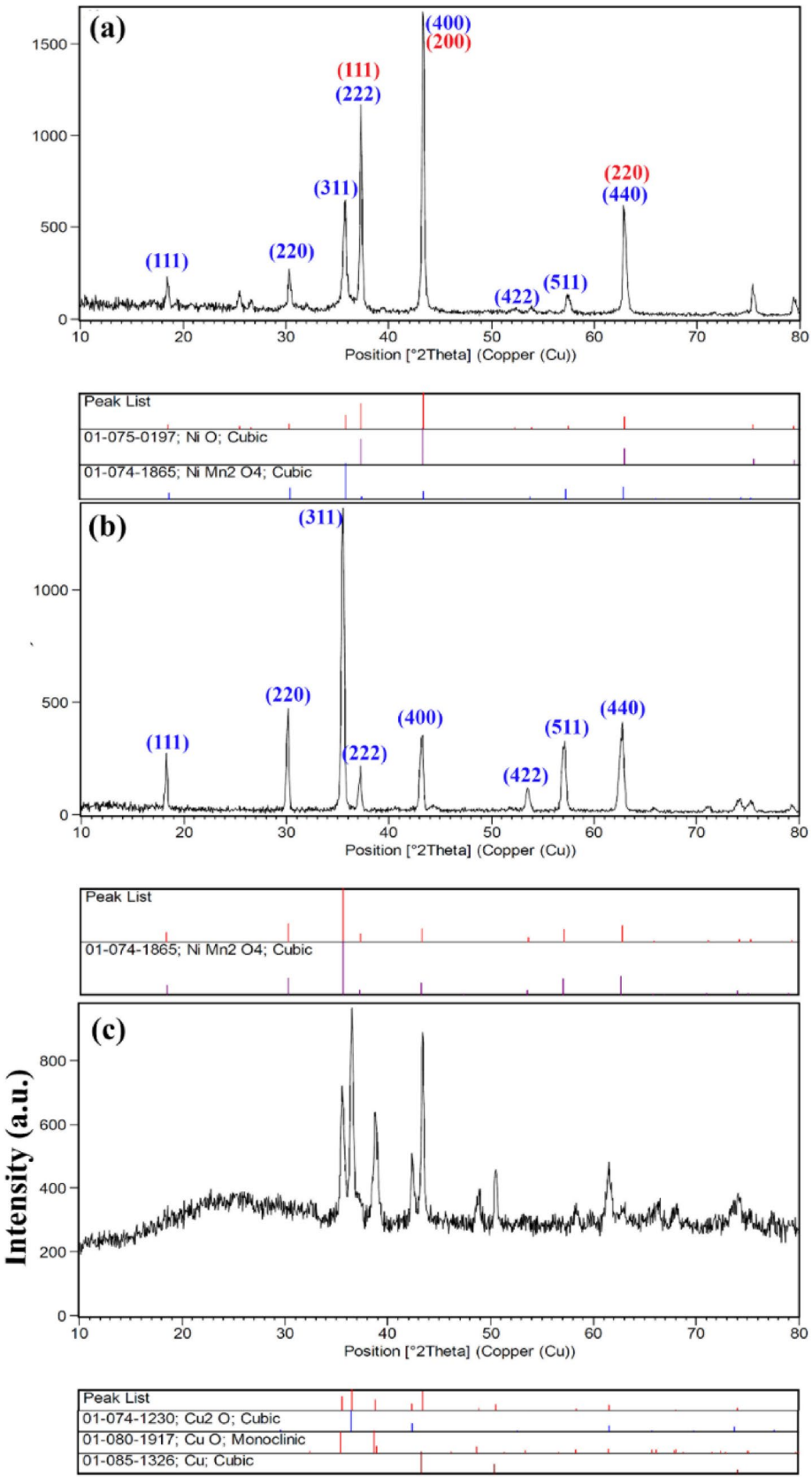


Fig. 1 XRD patterns of the products prepared from Ni and Mn salts after calcination at 850 ˚C for two h: **a** sample 1 (prepared with sucrose); **b** sample 2 (prepared with allium cepa), and **c** sample 4 (prepared from Ni, Cu, and Mn salts with sucrose)

prepared in the presence of allium cepa is the pure $NiMn_2O_4$ with the cubic crystal system and database in JCPDS card No. 01–074-1865. The peaks in this figure have been marked by their indices with blue color ((111), (220), (311), (222), (400), (422), (511) and (440)). In this research, we synthesized sample 4 using three metal salts, including Ni $(NO_3)_2.6H_2O$, Cu $(NO_3)_2.3H_2O$, and Mn $(NO_3)_2.4H_2O$, as precursors. The reaction conditions for the synthesis of sample 4 have been listed in Table 1. XRD pattern of sample 4 reveals formation of copper and copper oxides, as shown in Fig. 1c. The peaks in this figure are consistent with the databases in JCPDS cards No. 01–074-1230, 01–080-1917, and 01–085-1326 and reveal Cu_2O, CuO, and Cu with cubic, monoclinic, and cubic phases. No diffraction peak from nickel and copper manganites was detected in this figure. Therefore, sample 4 was not considered as the optimal product in this research.

Figure 2 shows the XRD patterns of samples 1 and 2 before calcination. No considerable difference is observed in the XRD patterns of samples 1 and 2 before calcination. No diffraction peaks are observed, indicate amorphous structures in both as-synthesized samples before calcination. To obtain pure metal manganites, calcination temperature and time must be controlled; otherwise, amorphous phases may form.

SEM and TEM images

The morphology of the $NiMn_2O_4$ nanostructures and Ni/Cu/CS nanocomposites was analyzed using SEM and TEM. The images were depicted in Figs. 3 and 4. The SEM images of $NiMn_2O_4$ (sample 2) are shown in Fig. 3a and b. In this figure, the nanorods with the diameter of 200–600 nm and nanoparticles with diameters less than 50 nm can be observed. We also investigated TEM images of the samples. TEM images in Fig. 3c and d show that diameter of the $NiMn_2O_4$ nanorods is less than 50 nm. The electrostatic configuration and surface composition of as-prepared products were evaluated by EDS. The EDS spectrum of sample 2 in Fig. 3e shows the presence of Ni, Mn, and O elements and confirms XRD results in Fig. 1b.

SEM images were also used to study the surfaces of the nanocomposites (absorbents). Figure 4a-d shows SEM images of synthesized Ni/Cu/CS nanocomposites with different ratios of Ni/Cu/CS. Figure 3a-d revealed that the pure $NiMn_2O_4$ displays agglomerated nanorods of regular shapes. Whereas, in SEM images of $NiMn_2O_4$ and $CuMn_2O_4$, added

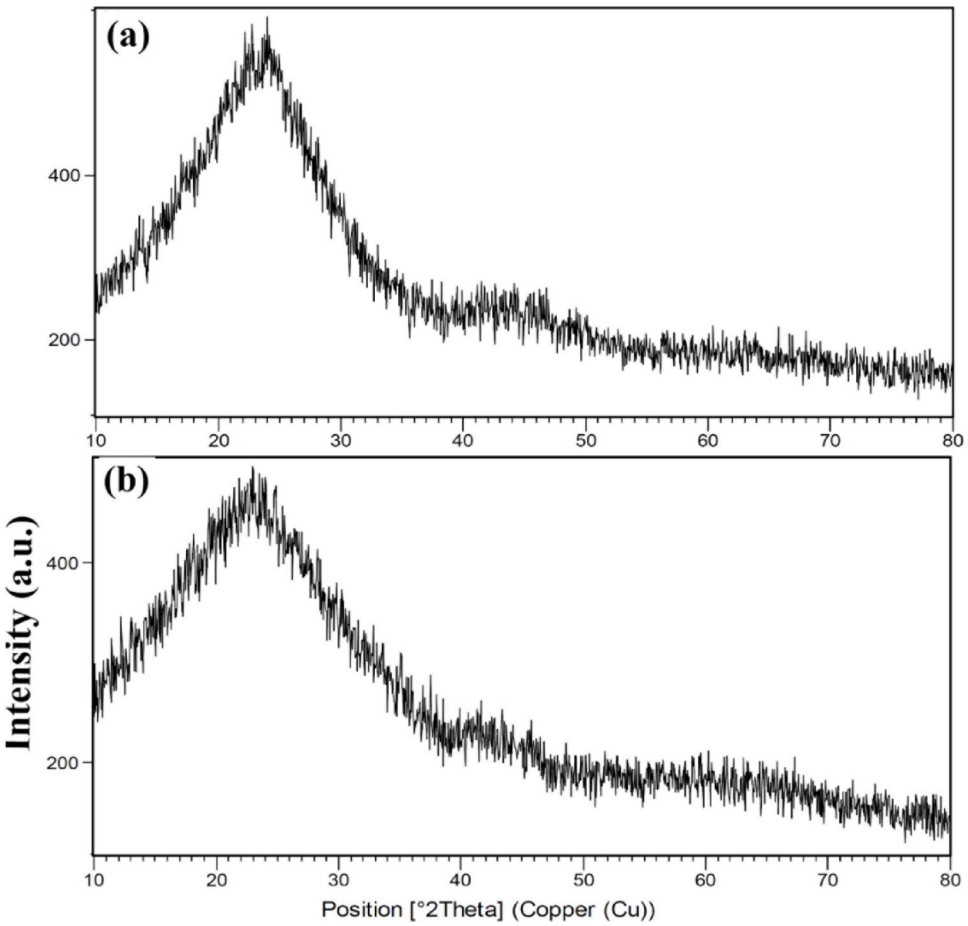


Fig. 2 XRD patterns of samples 1 and 2 before calcination

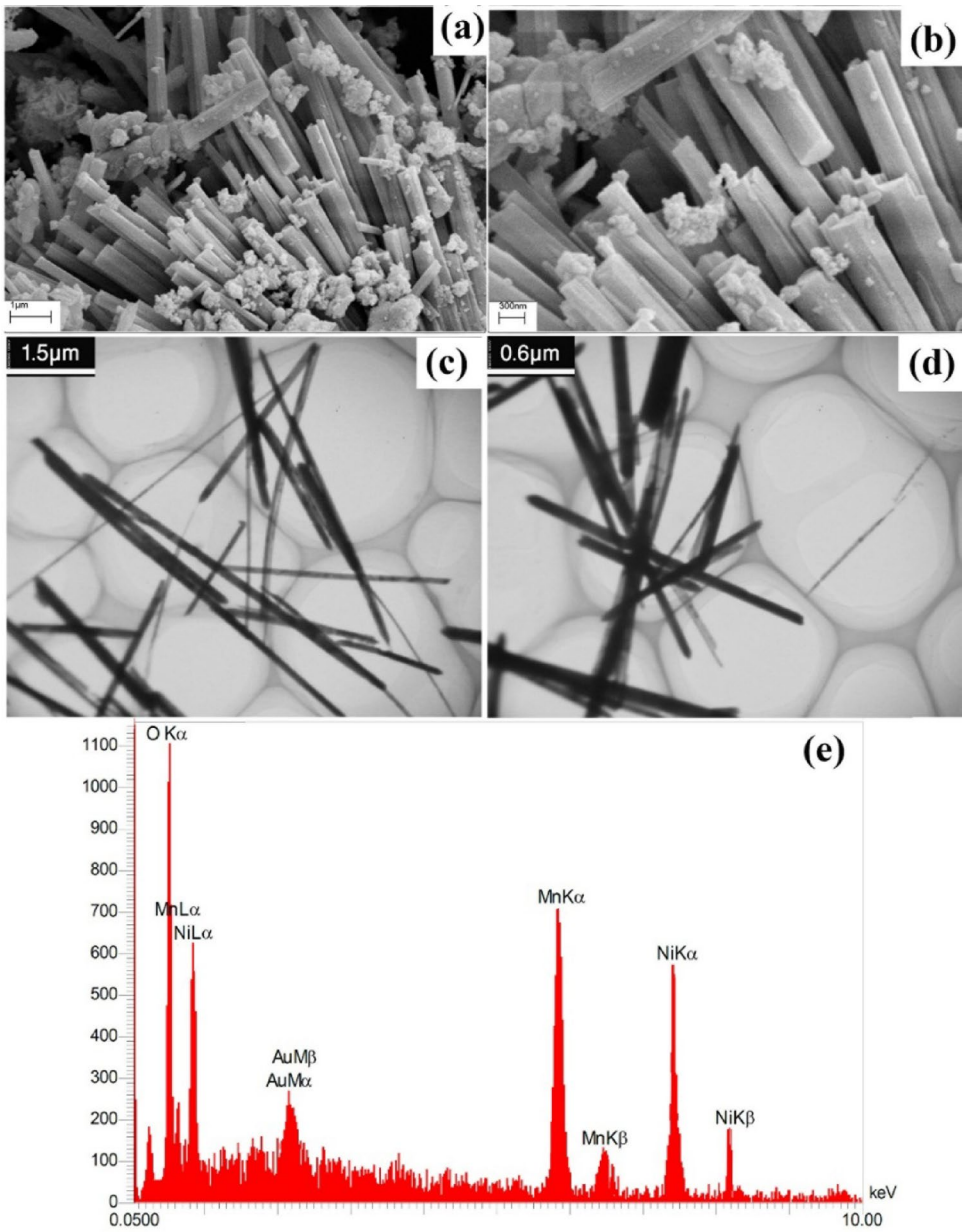


Fig. 3 **a**, **b** SEM images; **c**, **d** TEM images, and **e** EDS spectrum of $NiMn_2O_4$ (sample 2)

chitosan, agglomerated nanorods and nanostructures of irregular shapes are shown due to the aggregation phenomenon caused by chitosan (Fig. 4a-d). Figure 4 shows that $NiMn_2O_4$ nanoparticles and nanorods are embedded in the chitosan and unveils the composite formation of Ni/Cu/CS. The figure shows deep and irregular cavities. These indicate higher specific surface area, better energy distribution, and improved pollutant adsorption. Based on these images, it is found that the morphology of Ni/Cu/CS nanocomposites with 1:1:2 (sample 5) and 2:1:3 (sample 6) W/W ratios of Ni/Cu/CS, is almost the same. It implies that the weight ratios of Ni/Cu/CS do not much affect the morphology of the Ni/Cu/CS nanocomposites in the condition of the present work.

The presence of chitosan as well as NMO and CMO peaks is observed from the XRD pattern of Ni/Cu/CS nanocomposite which is shown in Fig. 4e. This figure shows the XRD pattern of sample 6. The pattern of chitosan-coated NMO and CMO reveals clear diffraction peaks in the relative intensity of both chitosan and nanostructures. The typical peaks of the chitosan membrane appear at 10.4 °, 12.8 °, and 19.9 ° (Kumar et al. 2012). These peaks are weakened and shifted in the XRD pattern of nanocomposites because the chitosan matrix is bound by nanostructures via the amine and hydroxyl groups. The presence of chitosan in the nanocomposites is observed at broad and weak peak at 2θ value at about 20°, as shown in Fig. 4e. The broad diffraction peak refers to the successful decoration of chitosan

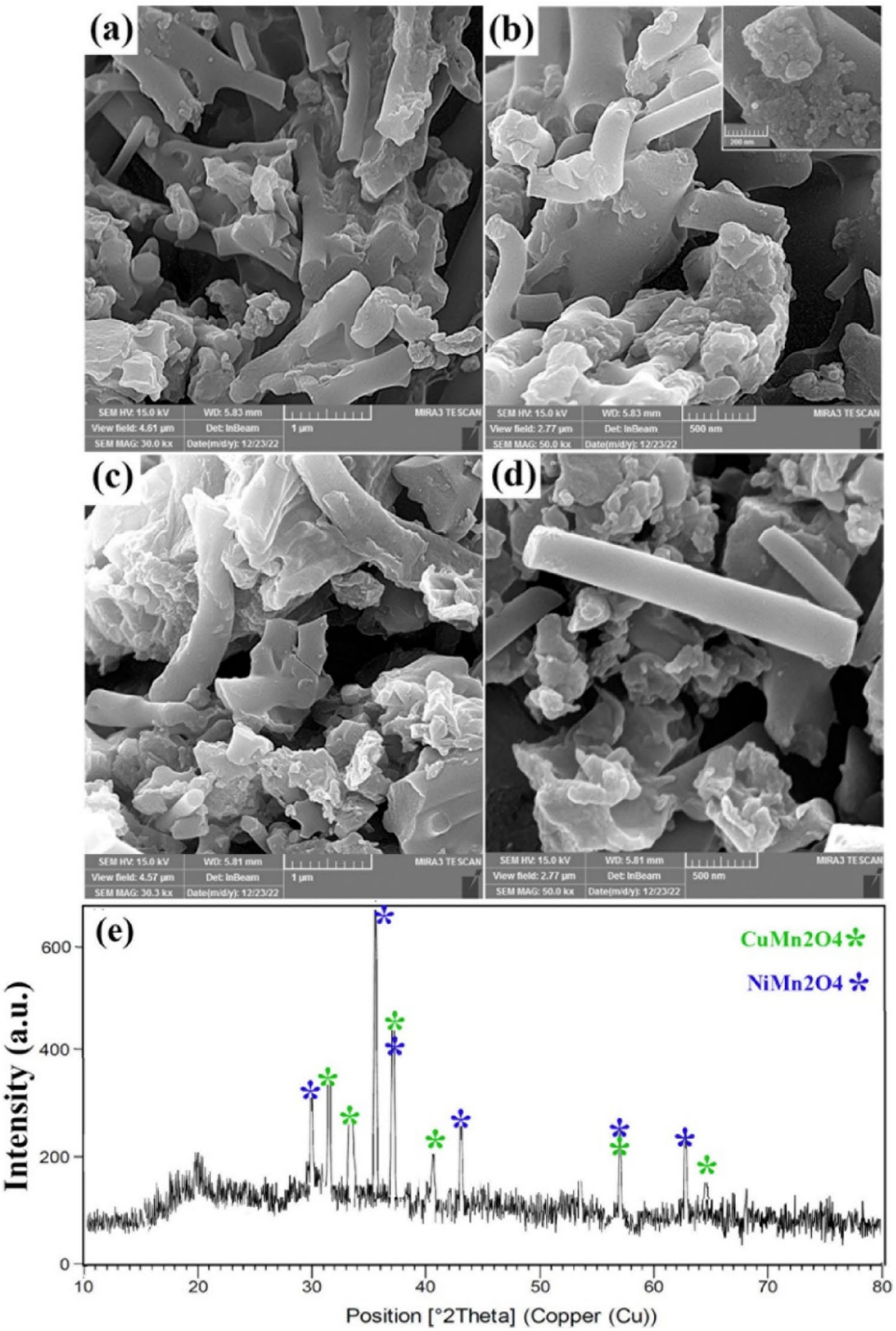


Fig. 4 SEM images of synthesized Ni/Cu/CS nanocomposites with different ratios of $NiMn_2O_4$:$CuMn_2O_4$: chitosan: **a**, **b** 1:1:2 (sample 5), insert: image at higher magnification, **c**, **d** 2:1:3 (sample 6), and **e** XRD pattern of sample 6

layer on the NMO and CMO surfaces. In this figure, other diffraction peaks marked with green and blue stars refer to $CuMn_2O_4$ and $NiMn_2O_4$ reinforced chitosan nanocomposite membranes, respectively. The cubic and monoclinic phases of $NiMn_2O_4$ and $CuMn_2O_4$ was indicated by comparison with JCPDS cards No. $NiMn_2O_4$; 01–074-1865, and $CuMn_2O$;00–010-0365. In Fig. 4e, the intensity of the XRD peaks shows a decrease when compared to pure $NiMn_2O_4$ (Fig. 1b) and $CuMn_2O_4$ (Fig. 1a in the author's published paper (Samadi Kazemi and Sobhani 2023). The figure indicates that nanostructures are embedded in the chitosan and unveils the formation of the Ni/Cu/CS nanocomposite. However, the shape and strength of the XRD peaks of the $NiMn_2O_4$ and $CuMn_2O_4$ can demonstrate that the nanostructures have a higher crystallinity than the nanocomposites. The order of polymer chains is impeded with the presence

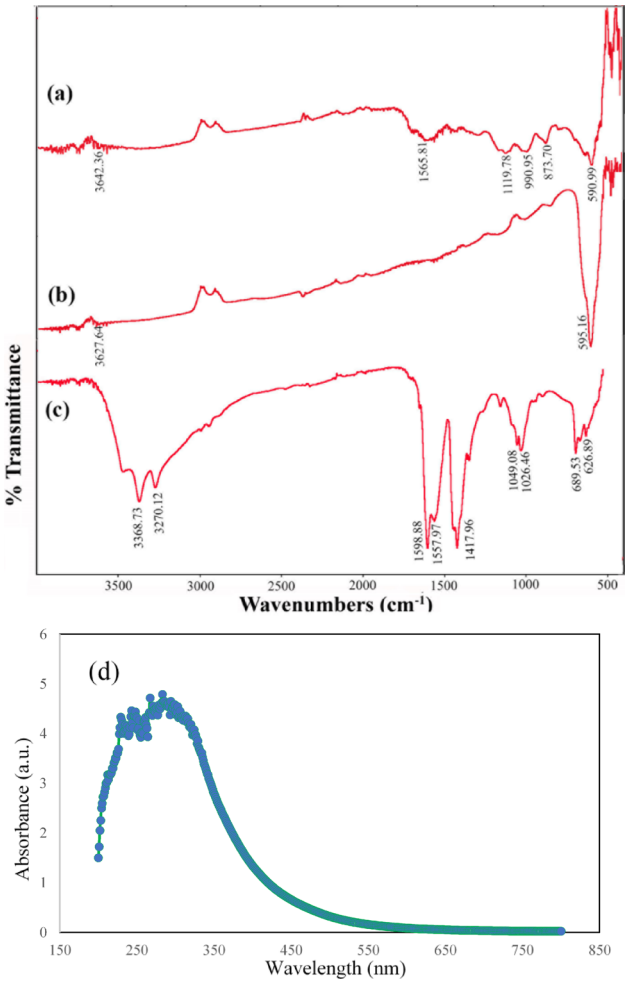


Fig. 5 FT-IR spectra of: **a** sample 1, **b** sample 2, **c** sample 6, and **d** UV–Vis spectrum of sample 2

of the nanostructures. So, introducing the nanostructures in chitosan is caused increasing the flexibility of the polymer chain and decreasing the crystallinity of composite membranes (Kumar et al. 2012).

FT-IR and UV-Vis spectra

The formation of NMO nanostructures and Ni/Cu/CS nanocomposites was also confirmed by FT-IR. In order to identify functional groups of the samples, the FT-IR spectra were recorded in the wavelength range 500–4000 cm^{-1}. The frequencies below 1000 cm^{-1} of low-frequency mode vibration frequencies belong to the metal-oxygen stretching vibrations (Wang et al. 2013). In Fig. 5a and b, the peaks at 590.99 and 595.16 cm^{-1} are related to the stretching vibrations of Mn–O, Ni–O and Cu–O bonds in samples 1 and 2. The weak peak at about 3600 cm^{-1} in Fig. 5a and b is related to the stretching vibrations of absorbed water on the surface of nanostructures. Also, the bands at about 990.95 cm^{-1} and 1565.81 cm^{-1} in Fig. 5a are attributed to the OH…O

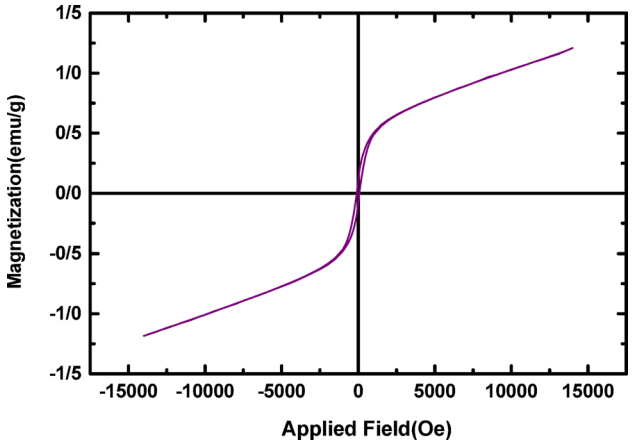


Fig. 6 Hysteresis curve of sample 2. (Inset: aAn enlarged illustration of the hysteresis curve)

hydrogen-bonding and O–H bending vibrations of the water, respectively. Figure 5c displays the FT-IR spectrum of Ni/Cu/CS nanocomposites. It can be seen that bands related to the NMO in nanocomposites form. The absorption peaks at 626.89 cm^{-1} and 689.53 cm^{-1} are associated with Ni–O, Mn–O, and Cu–O bonds in the as-prepared nanocomposites (Pramothkumar et al., 2019). These peaks are slightly shifted compared to the NMO. In Fig. 5c three bonds at 1417.96, 1049.08 and 1026.46 cm^{-1} corresponds to C–OH groups, organic residues in the nanocomposites (Ma et al. 2016). In this figure, the peaks at 1598.88 and 1557.97 cm^{-1} are related to C═O and CO vibrations. Also, the broad peak in the range 3200–3600 cm^{-1} (including 3368 and 3270 cm^{-1}) corresponds to the stretching vibrations of absorbed water on the surface of the nanocomposites. Figure 5d shows the UV-vis spectrum of sample 2, $NiMn_2O_4$. This figure shows a broad absorbance band in the range from 200 to 350 nm. The UV-Vis results agree with those obtained by other researchers (Rohokale et al. 2021; Sedighi et al. 2019).

Magnetic property

Figure 6 shows a plot of the magnetization versus magnetic field for NMO NSs. The curve shows a ferromagnetic behavior for the NSs with Hc at 171.71 Oe. The enlarged illustration of hysteric loop has been demonstrated in Inset of Fig. 6.

Adsorption isotherm and kinetic adsorption studies

We investigated the process mechanism and adsorption capacity of Ni/Cu/CS nanocomposites for MO removal using kinetic adsorption and adsorption isotherm experiments. Also, we investigated the experiments in the different times. As shown in Fig. 7a, the removal percentage

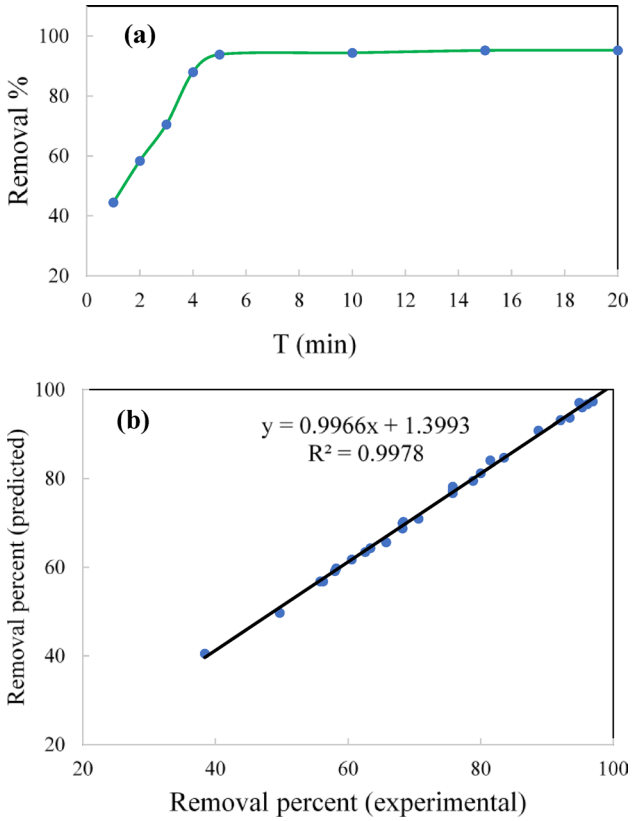


Fig. 7 **a** Effect of contact time on the removal efficiency of MO by Ni/Cu/CS in the ambient temperature, **b** Plot of the experimental results versus the predicted results of the model for MO removal percent

increases steeply but remains constant after 5 min reaching equilibrium.

The comparison of the experimental results of MO removal with the results obtained from the model is drawn in Fig. 7b. The R^2 amount of more than 0.8, refers that the empirical data's desired agreement with the obtained one by the relevant equations (Fereidonian Dashti et al. 2018).

The result show (Table 4), the $R^2_{predicated}$ (0.9739) is close to the $R^2_{adjusted}$ (0.9975). A difference of less than 0.2 between indicates the fitting of the model (Li et al. 2021). The F-value of Lack of Fit is 3.51, which shows it is not significant, and this is desirable for the model. As shown in Fig. 7b, the R^2 value from experimental versus predicted MO removal is close to 1, confirming the model's validity.

The variance analysis of MO removal was based on adsorbent dosage, dye concentration, pH, contact time, and agitation speed. These parameters were studied as experimental variables. The results have been summarized in Table 4. F-values more than five and P-values lower than 0.05 prove that the parameters are essential in the model (Masoumi et al. 2021). A, B, C, D, E, AB, AC, AD, AE, BC, BD, BE, CD, CE, DE, A^2, B^2, C^2, D^2, E^2 are significant model terms.

We obtained the equation to predict the optimum point according to the central composite design and input variables. Then, we presented the empirical relationship between the response and the independent variables in the coded units based on the experimental results as follows (Eq. 1):

$$\begin{aligned}\text{MO removal}\% = {} & 76.77 - 2.11\,A - 2.60B + 10.15\,C - 3.45D + 5.93E + 5.69AB \\ & - 1.44AC + 3.93ADAD - 1.89AE + 4.99BCBC - 2.38BD + 4.72BE + 4.08CD \\ & - 4.82CECE + 1.65DE + 18.88A^2 - 12.65B^2 + 14.25C^2 - 9.15D^2 - 13.57E^2\end{aligned} \quad (1)$$

The perturbation diagram obtained from Design-Expert software shows the effect of variables on the response. A positive slope means a positive impact on the response, a negative slope means an adverse impact, and a zero slope means that the variable does not affect on the reaction. The plot of perturbation for removal of MO solution with Ni/Cu/CS was shown in Fig. 8.

In this study, three-dimensional graphs of the response surface to show the changes in response against factors are illustrated in Fig. 9a–d.

As shown from Figs. 8 and 9, the studied factors are interdependent and according to Eq. 1. The adsorption process was optimized by central composite design (CCD) found in the response surface methodology of the Design-Expert software. In the optimal conditions, the amount of adsorbent, pH, initial concentration, contact time and agitation speed were obtained as 1.2 g/L, 3, 10 mg/L, 5 min and 300 rpm, respectively.

The MO removal percent at time t, the adsorption capacity (q_t, mg/g) at time t, and the adsorption capacity at equilibrium (q_e, mg/g) are described by Eqs. 2–4 (Far et al. 2020; Gollakota et al. 2021; Khan et al. 2021; Wang et al. 2020).

$$Removal\% = \frac{C_0 - C_t}{C_0} \times 100 \quad (2)$$

$$q_t = \frac{C_0 - C_t}{m} \times V \quad (3)$$

$$q_e = \frac{C_0 - C_e}{m} \times V \quad (4)$$

C_0, C_t, and C_e are concentrations (mg/L) at initial, t, and equilibrium times, respectively. q_t, q_e, V, and m are the adsorption capacity (mg/g) at t and equilibrium times, the volume (L) of the solution, and the amount (g) of adsorbent material used, respectively.

Examining the kinetic behavior of adsorption provides information about the equilibrium state. Table 5 presents

Table 4 ANOVA values in the RSM-CCD model for MO removal with Ni/Cu/CS

Source	Sum of squares	df	Mean square	F-value	*p*-value	
Model	7291.09	20	364.55	543.48	<0.0001	Significant
A-Time	80.48	1	80.48	119.97	<0.0001	
B-Adsorbent dose	122.15	1	122.15	182.10	<0.0001	
C-pH	1856.03	1	1856.03	2766.96	<0.0001	
D-Speed	213.76	1	213.76	318.68	<0.0001	
E-Initial concentration	632.38	1	632.38	942.74	<0.0001	
AB	517.79	1	517.79	771.92	<0.0001	
AC	33.12	1	33.12	49.38	<0.0001	
AD	247.75	1	247.75	369.34	<0.0001	
AE	57.30	1	57.30	85.43	<0.0001	
BC	398.40	1	398.40	593.94	<0.0001	
BD	90.35	1	90.35	134.69	<0.0001	
BE	355.89	1	355.89	530.56	<0.0001	
CD	266.18	1	266.18	396.82	<0.0001	
CE	371.14	1	371.14	553.29	<0.0001	
DE	43.43	1	43.43	64.74	<0.0001	
A^2	877.45	1	877.45	1308.10	<0.0001	
B^2	393.89	1	393.89	587.22	<0.0001	
C^2	499.92	1	499.92	745.27	<0.0001	
D^2	206.11	1	206.11	307.26	<0.0001	
E^2	453.26	1	453.26	675.72	<0.0001	
Residual	7.38	11	0.6708			
Lack of fit	5.96	6	0.9939	3.51	0.0947	Not significant
Pure error	1.42	5	0.2831			
Cor total	7298.46	31				

$R^2 = 0.9992$

$R^2_{adjusted} = 0.9975$

$R^2_{predicated} = 0.9739$

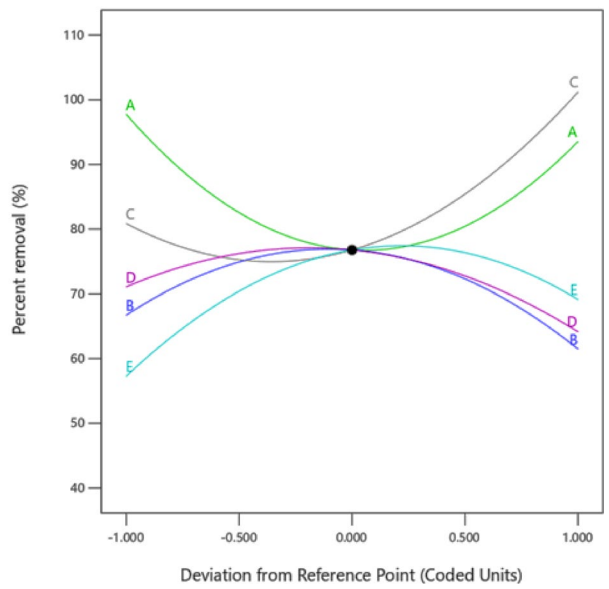


Fig. 8 Plot of perturbation for the effective variables of MO removal percent with Ni/Cu/CS

the kinetic results of MO adsorption using different models. As shown in Table 5, the pseudo-second-order model best fitted the experimental data ($R^2 = 0.9964$). This model suggests that surface resistance is not the rate-limiting step. The adsorption occurs in two stages: a rapid initial step, followed by a slower step limited by dye diffusion into smaller pores. It means that the amount of absorption is proportional to the square of the number of empty pores remaining in the absorbent sites (Foo and Hameed 2012).

The isotherm parameters of MO by Ni/Cu/CS are listed in Table 3. By comparing the value of R^2 for different models in Table 3, it is clear that the Langmuir model (0.9999) is more consistent with experimental data than other models. Assumptions in the Langmuir model include: (1) monolayer absorption for the absorbent surface and (2) the same tensile strength for all centers and absorption sites for MO. Also, the optimal K_L value for the adsorption process based on the Langmuir model is 0–1, which was obtained at 0.01 in this investigation.

The point of zero charge (pH_{pzc}) is the point at which the surface charge of the adsorbent is neutral. To determine adsorbent pH by the drift method, 10 mL of sodium chloride

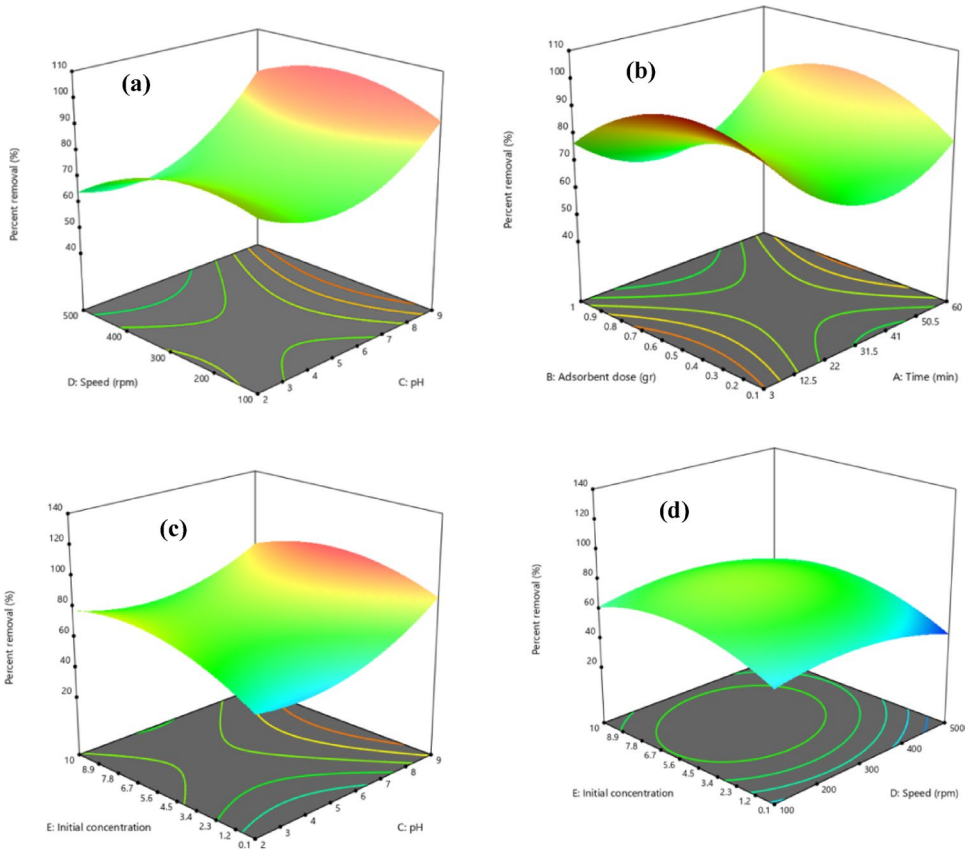


Fig. 9 Three-dimensional graph for: **a** influence of pH and agitation speed **b** influence of contact time and adsorbent dosage **c** influence of initial concentration and pH **d** influence of initial concentration and agitation speed on MO removal percent

Table 5 Kinetic parameters of MO adsorption on Ni/Cu/CS

Model	Parameter	Value
Pseudo-first-order; $Ln\,(q_e - q_t) = Ln\,(q_e) - K_1 t$	K_1 (min^{-1})	0.7003
	R^2	0.8962
Pseudo-second-order; $\frac{t}{q_t} = \frac{1}{K_2 q_e^2} + \frac{t}{q_e}$	K_2 (g mg^{-1} min^{-1})	2.33
	R^2	0.9964
Intra-particle diffusion; $K_{id}t^{1/2} + C_{id}$	K_{id} (mg g^{-1} $min^{-1/2}$)	0.6721
	R^2	0.6363
Elovich; $q_t = \alpha + \beta\, Ln\, t$	α (mg $g^{-1}min^{-1}$)	2.5557
	β (g min^{-1})	0.8632
	R^2	0.8024

k1 Pseudo-first-order kinetic rate constant, *k2* Rate constant of pseudo-second-order kinetic, *kid* Intra-particle diffusion rate constant, *Cid* Intra-particle diffusion constant

solution was placed in separate containers and adjusted to eight pH levels (2–9). We used sodium hydroxide and hydrochloric acid to adjust the solution pH. Then 0.05 g of absorbent was added to the solutions, and the samples were placed in the shaker at 300 rpm. After 24 h, the adsorbent was separated from the solution, and the pH was measured again.

The absorption mechanism depends on the characteristics and nature of the adsorbent and the adsorbate material. MO is an aromatic compound that binds to the adsorbent through electrophilic interactions, π-π interactions, and hydrogen bonding via its N and S atoms (Igwegbe et al. 2023). On the other hand, MO is an ionizable molecule with a pKa of 3.4, so it can form electrostatic interactions with adsorbents that are not at their isoelectric point. The adsorbent used in this work is spinel metal oxide embellished on the surface of chitosan. Chitosan is a weak base and can form hydrogen bonds because of the presence of amine and hydroxyl groups. Chitosan can provide a steric barrier with a positive charge density, leading to strong electrostatic interactions among nanostructures and MO (Phan et al. 2021).

Figure 10a shows the UV-Vis spectrum of the MO solution before and after passing through the absorbent in the region of 200–800 nm. The maximum wavelength for MO is 464nm; the disappearance of the peak after passing through the absorber indicates the absorption of MO by the absorbent.

Figure 10b shows the pH_{pzc} = 7 for the adsorbent. This value is obtained by the drift method. At pH lower than pH_{pzc}, the absorbent surface is positive, while at pH greater than pH_{pzc}, the absorbent surface is negative. Therefore, the electrostatic interactions between the MO solution and the adsorbent are expected to be higher at acidic pH. Based on the obtained model and experimental results the optimal pH for maximum removal was at pH = 3.

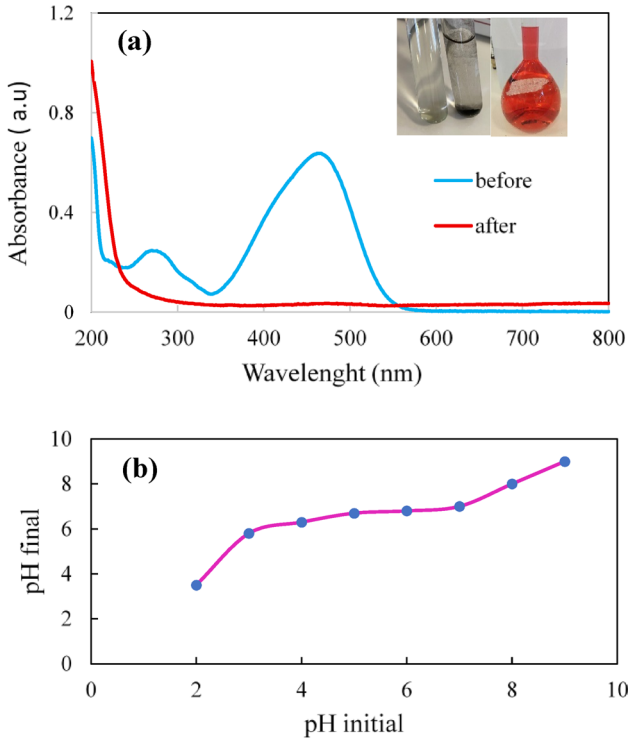


Fig. 10 **a** The absorbance spectra of MO (before) and MO adsorbed on the surface of Ni/Cu/CS (after), **b** pH_{pzc} of the adsorbent of Ni/Cu/CS

In Table 6, the performances of Ni/Cu/CS for MO adsorption were compared to the other adsorbents reported in the literature. The maximum adsorption capacity of Ni/Cu/CS was lower than AC from waste tire rubber (q_{max} = 588.0) and CoAl/Cl LDH (q_{max} = 827.5) but its removal efficiency was higher. Ni/Cu/CS showed higher removal efficiency and maximum capacity for MO than other adsorbents in Table 6. Chitosan-based adsorbents play an essential role in removing organic pollutants from wastewater. This is due to their unique physicochemical properties.°

Table 7 compares the maximum adsorption capacity of Ni/Cu/CS with other adsorbents. It also shows the contact time for MO adsorption reported in the literature. The adsorption capacity of the composite in this work is 416.67 mg/g. It is very high, although slightly lower than that reported by Chen et al. (Chen et al. 2024). Also, the adsorption rate of the present work is high. After 5 min, our group work achieves ultra-fast removal, far faster than the 2–4 h required in other systems. Inclusion of onion extract in synthesis (biogenic green chemistry), combined with magnetic properties (from $NiMn_2O_4$) for easy recovery, stands out.

The SEM images in Fig. 4c and d were related before adsorption, while Fig. 11a and b highlight the SEM images after MO dye adsorption. The pictures in Fig. 4 show pores that allow MO to adhere to its surface. Also, these images show the bright spots and the adsorbent's rough, porous surface, which enhances adsorption capacity. Figure11 shows that the dye covered the adsorbent's pores, voids, caves, and surfaces. The images obtained of the adsorbents before and after absorption confirm that they can absorb the pollutants due to their specific surface area. The SEM images of the adsorbent after the adsorption show the presence of many unfilled active sites. The available active sites mean the adsorbent can be reused several times in the continuous adsorption system. Figure 11c shows the FTIR spectrum of the adsorbent after MO adsorption. There is a difference in the FT-IR before (Fig. 5c) and after the dye adsorption. The FT-IR spectrum of the nanocomposite after MO adsorption shows that the bands are blue-shifted. It suggests that the functional groups on MO are linked to the Ni/Cu/CS.

We studied the desorption and regeneration of the adsorbent. The solvents used were distilled water (H_2O), nitric acid (HNO_3), hydrochloric acid (HCl), acetone ($(CH_3)_2CO$), ethanol (C_2H_5OH), and sodium hydroxide (NaOH). The highest dye desorption efficiency (78%) was earned with HCl and HCl solution with 0.1 M concentration was selected as a suitable desorbing agent. Figure 12 shows that the adsorbent can be reused for up to five cycles. After seven cycles, MO adsorption decreased to 42%.

Table 6 Comparison of the adsorption performance of MO by Ni/Cu/CS with other adsorbents

Adsorbent	Highest RE%	q_{max} mg/g	pH	T $(°C)$	Method of q_{max} determination	Reference
AC from waste tire rubber	80	588.0	3.6	23	Langmuir	(Islam et al. 2018)
AC from aloe vera	-	196.1	3	25	Langmuir	(Zhang et al. 2020)
Biochar from chicken manure	100	41.49	6.5	45	Langmuir	(Yu et al. 2018)
CoAl/Cl LDH	90.5	827.5	7	25	Langmuir	(Chen et al. 2019)
HDPyβ-clay	-	227.3	3	-	Langmuir	(Gamoudi and Srasra 2019)
Cd-zeolite imidazolate framework (Cd-ZIF-8)	92	145.4	2	50	Langmuir	(Gamoudi and Srasra 2019)
Chitosan/β-cyclodextrin polymer	-	398.8	-	-	Langmuir	(Jiang et al. 2018)
Chitosan/$Fe(OH)_3$ beads	91.1	314.5	3	25	Langmuir	(XinxinYang et al., 2018)
Chitosan/PVA/TiO_2 nanofiber	94	314.0	-	-	Langmuir	(Habiba et al. 2019)
Chitosan/bentonite	-	141.2	11	23	Langmuir	(Zhang et al. 2016)
Cetyltrimethylammonium bromide/H_2O_2-clay	98	268.7	3	25	Dubinin-Radushkevich	(Mobarak et al. 2018)
Ni/Cu/CS nanocomposite	99.3	416.67	3	25	Langmuir	This work

T Temperature

Table 7 Comparison of maximum adsorption capacity and contact time for MO adsorption by Ni/Cu/CS and other researchers

Adsorbent	Max. adsorption capacity (mg/g)	Contact time	Key features	Reference
Chitosan–Palmer Amaranth Biochar composite microspheres	495–554	~240 min	High adsorption, multiple cycles (93.6% retention after 5), broad interactions (MDPI)	(Chen et al. 2024)
Modified magnetic chitosan microspheres	486.13 at 125 mg/L MO	~120 min	Magnetic, high capacity, good removal efficiency (PMC)	(Wang et al. 2025)
Pure chitosan beads	12.46	unspecified, likely longer	Simple system, some regeneration (87.2% after three cycles) (MDPI)	(Alyasi et al. 2023)
Ni/Cu/CS nanocomposite	416.67	5 min	Green synthesis, magnetic, comprehensive characterization	Your work

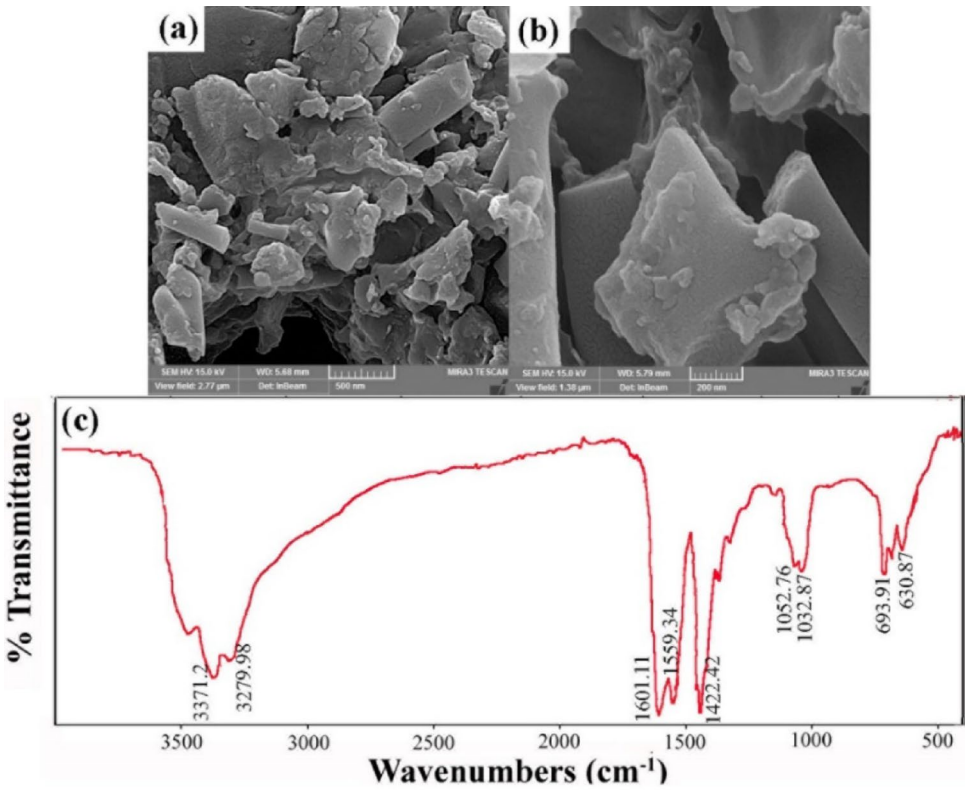


Fig. 11 **a**, **b** SEM images and **c** FT-IR spectrum of sample 6 after adsorption of MO

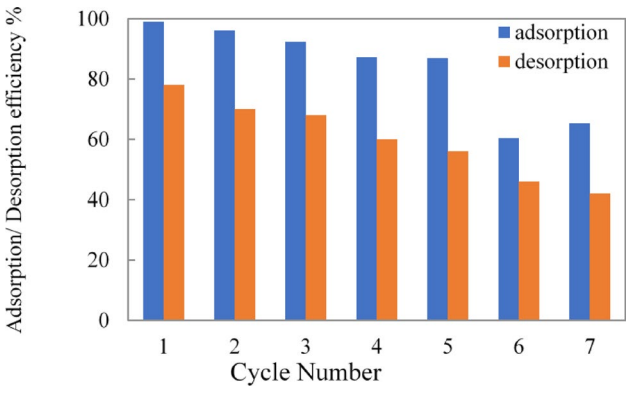
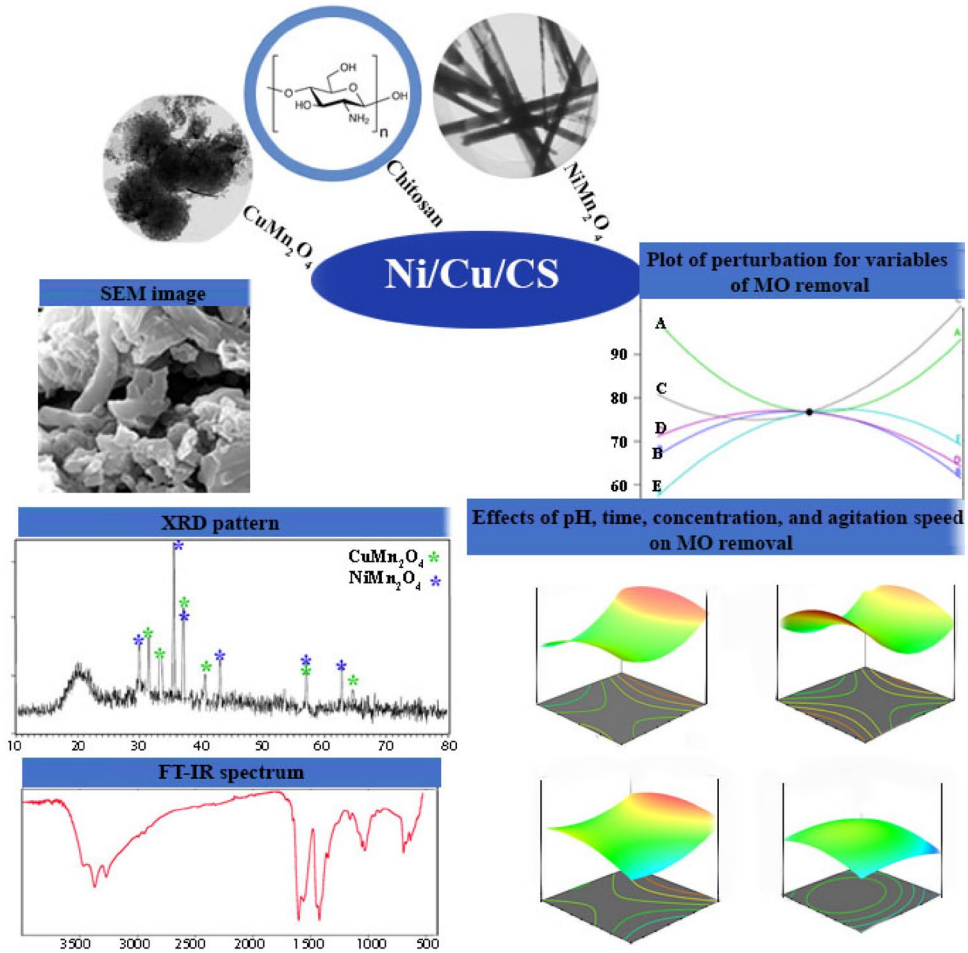


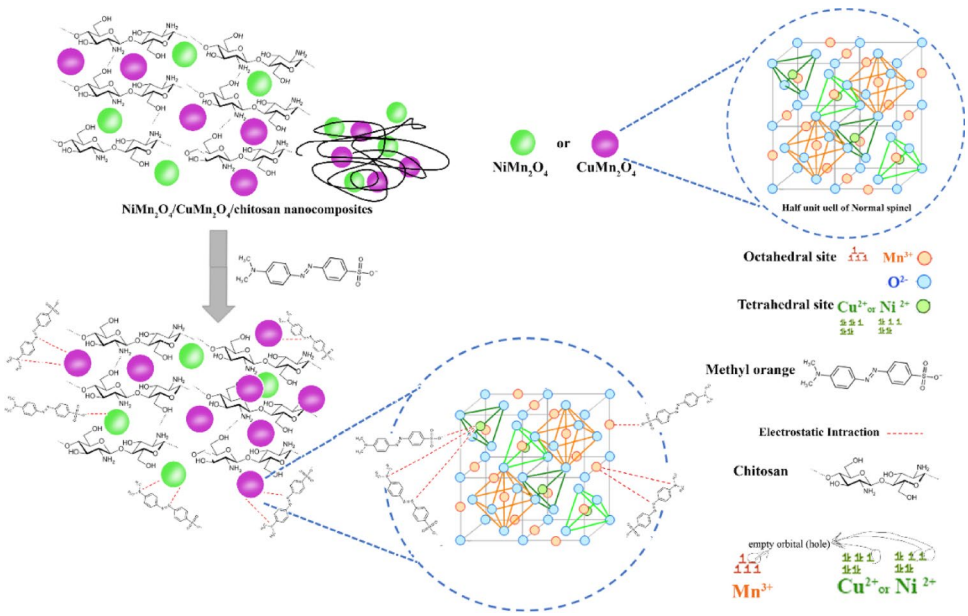
Fig. 12 Plot adsorption/desorption of MO versus cycle number (contact time = 5 min, initial dye concentration = 10 mg/L, solvent = HCl, and adsorbent dosage = 1.2 g/L)

Scheme 1 shows a schematic diagram of the characterization and applications of Ni/Cu/CS nanocomposites.

Scheme 2 shows a schematic diagram of the adsorption mechanism of MO on Ni/Cu/CS nanocomposites. The strengths of our work are listed below. (1) Using Allium cepa as a bio-based agent makes the synthesis environmentally friendly, which is a clear advantage over many studies relying on toxic chemicals. (2) The combination of $NiMn_2O_4$/$CuMn_2O_4$/chitosan is relatively unique. Most published works focus on either binary systems or single metal oxides, so the ternary hybrid offers novelty. (3) A maximum adsorption capacity of 416.67 mg/g for methyl orange is very high compared to many reported adsorbents (typically 100–300 mg/g). (4) The ultra-fast removal within 5 min is a



Scheme 1 Schematic diagram of the synthesis and investigation of the adsorption kinetics of Ni/Cu/CS



Scheme 2 Schematic diagram of the adsorption mechanism of MO on Ni/Cu/CS nanocomposites

significant advantage since most comparable studies report equilibrium times of 30–120 min. (5) The use of multiple techniques (XRD, SEM, TEM, FTIR, UV-Vis, VSM, EDS) provides strong evidence for structural and functional confirmation of the nanocomposite. (6) The observed ferromagnetic properties facilitate easy separation after adsorption, an essential feature for practical wastewater treatment.

Conclusion

NMO and CMO were successfully synthesized using Allium cepa via a hydrothermal route, and a new Ni/Cu/CS nanocomposite was obtained by stirring at room temperature. SEM and XRD confirmed the formation of nanocomposites with embedded nanoparticles in the chitosan matrix, showing enhanced surface cavities, good structural stability, and shifted diffraction peaks. VSM revealed ferromagnetism (Hc = 171.71 Oe), while UV-Vis indicated favorable optical properties. Ni/Cu/CS was effectively applied for MO removal, achieving a maximum adsorption capacity of 416.67 mg/g with high correlation to the Langmuir model (R^2 = 0.9964, KL = 0.01), following a pseudo-second-order mechanism. Optimum conditions were 1.2 g/L adsorbent, 10 mg/L dye, 5 min contact time, 300 rpm, and pH = 3.

Acknowledgements The authors are grateful to the Kosar University of Bojnord for supporting this work.

Author contributions Study conception and design: A. Sobhani. Experiments: Z. Izanloo. Data collection: A. Sobhani, M. Samadi Kazemi. Analysis and interpretation of results: A. Sobhani, M. Samadi Kazemi. Draft manuscript preparation: A. Sobhani.

Funding The authors are grateful to the Kosar University of Bojnord for supporting this work.

Data availability The authors declare that all relevant data that support the findings of this study are available within the article. Additional data are available from the corresponding author upon reasonable request.

Declarations

Conflict of interest The authors declare that they have no known competing financial interests or personal relationships that could have appeared to influence the work reported in this paper.

Ethical approval Not applicable.

Consent to participate Not applicable.

Consent for publication Not applicable.

Open Access This article is licensed under a Creative Commons Attribution 4.0 International License, which permits use, sharing, adaptation, distribution and reproduction in any medium or format, as long as you give appropriate credit to the original author(s) and the source, provide a link to the Creative Commons licence, and indicate if changes were made. The images or other third party material in this article are included in the article's Creative Commons licence, unless indicated otherwise in a credit line to the material. If material is not included in the article's Creative Commons licence and your intended use is not permitted by statutory regulation or exceeds the permitted use, you will need to obtain permission directly from the copyright holder. To view a copy of this licence, visit http://creativecommons.org/licenses/by/4.0/.

References

Ahmad MA, Alrozi R (2011) Removal of malachite green dye from aqueous solution using rambutan peel-based activated carbon: Equilibrium, kinetic and thermodynamic studies. Chem Eng J 171(2):510–516. https://doi.org/10.1016/j.cej.2011.04.018

Ahmad R, Ansari K (2021) Comparative study for adsorption of congo red and methylene blue dye on chitosan modified hybrid nanocomposite. Process Biochem 108:90–102. https://doi.org/10.1016/j.procbio.2021.05.013

Ahmadipouya S, Heidarian Haris M, Ahmadijokani F, Jarahiyan A, Molavi H, Matloubi Moghaddam F, Rezakazemi M, Arjmand M (2021) Magnetic Fe3O4@UiO-66 nanocomposite for rapid adsorption of organic dyes from aqueous solution. J Mol Liq 322:114910. https://doi.org/10.1016/j.molliq.2020.114910

Alaqarbeh M, Khalili F, Bouachrine M, Alwarthan A (2023) Synthesis, characterization and investigation of cross-linked chitosan/(MnFe2O4) nanocomposite adsorption potential to extract U(VI) and Th(IV). Catalysts 13(1):47

Alyasi H, Mackey H, McKay G (2023) Adsorption of methyl orange from water using chitosan bead-like materials. Molecules. https://doi.org/10.3390/molecules28186561

Amini R, Nabiyouni G, Jarollahi S (2021) Removal of azo dyes pollutants: photo catalyst and magnetic investigation of iron oxide-zinc sulfide nanocomposites. J Nanostruct 11(1):95–104. https://doi.org/10.22052/JNS.2021.01.011

Bayat S, Sobhani A, Salavati-Niasari M (2018) Co2SiO4 nanostructures/nanocomposites: synthesis and investigations of optical, magnetic, photocatalytic, thermal stability and flame retardant properties. J Mater Sci Mater Electron 29(9):7077–7089. https://doi.org/10.1007/s10854-018-8695-y

Beshkar F, Al-Nayili A, Amiri O, Salavati-Niasari M, Mousavi-Kamazani M (2022) Fabrication of S-scheme ZnO/Zn3(PO4)2 heterojunction photocatalyst toward photodegradation of tetracycline antibiotic and photocatalytic mechanism insight. Int J Hydrog Energy 47(2):928–939. https://doi.org/10.1016/j.ijhydene.2021.10.060

Carreño Hernández G, Pulido Melián E, Santiago DE (2025) Synthesis of activated carbon from sewage sludge using phosphoric acid as activating agent. Environ Sci Pollut Res. https://doi.org/10.1007/s11356-025-36516-y

Chani MTS, Karimov KS, Khan SB, Fatima N, Asiri AM (2019) Impedimetric humidity and temperature sensing properties of chitosan-CuMn2O4 spinel nanocomposite. Ceram Int 45(8):10565–10571. https://doi.org/10.1016/j.ceramint.2019.02.122

Chen Y, Jing C, Zhang X, Jiang D, Liu X, Dong B, Feng L, Li S, Zhang Y (2019) Acid-salt treated CoAl layered double hydroxide nanosheets with enhanced adsorption capacity of methyl orange dye. J Colloid Interface Sci 548:100–109. https://doi.org/10.1016/j.jcis.2019.03.107

Chen G, Yin Y, Zhang X, Qian A, Pan X, Liu F, Li R (2024) Enhanced adsorption of methyl orange from aqueous phase using

chitosan–palmer amaranth biochar composite microspheres. Molecules. https://doi.org/10.3390/molecules29081836

Chen R, Meng J, Tan S, Liang L, Wang F, Liu H, Guo C, Bao W, Zhang G, Yu F (2025) Plasma-assisted regeneration of activated carbon: current status and prospects. Inorganics. https://doi.org/10.3390/inorganics13070209

Dinh VP, Nguyen MD, Nguyen QH, Do TT, Luu TT, Luu AT, Tap TD, Ho TH, Phan TP, Nguyen TD, Tan LV (2020) Chitosan-MnO(2) nanocomposite for effective removal of Cr (VI) from aqueous solution. Chemosphere 257:127147. https://doi.org/10.1016/j.chemosphere.2020.127147

Etana R, Angassa K, Getu T (2025) Dye removal from textile wastewater using scoria-based of vertical subsurface flow constructed wetland system. Sci Rep 15(1):949. https://doi.org/10.1038/s41598-024-79174-9

Far HS, Hasanzadeh M, Nashtaei MS, Rabbani M, Haji A, Hadavi Moghadam B (2020) PPI-dendrimer-functionalized magnetic metal–organic framework (Fe3O4@MOF@PPI) with high adsorption capacity for sustainable wastewater treatment. ACS Appl Mater Interfaces 12(22):25294–25303. https://doi.org/10.1021/acsami.0c04953

Fayad E, Binjawhar DN, Elsaid FG, Taha A, Mubarak MF (2025) Innovative CuZnCr-BTC framework for enhanced Congo red dye removal in sustainable wastewater treatment. J Clust Sci 36(4):125. https://doi.org/10.1007/s10876-025-02840-z

Feng M, Yu S, Wu P, Wang Z, Liu S, Fu J (2021) Rapid, high-efficient and selective removal of cationic dyes from wastewater using hollow polydopamine microcapsules: isotherm, kinetics, thermodynamics and mechanism. Appl Surf Sci 542:148633. https://doi.org/10.1016/j.apsusc.2020.148633

Fereidonian Dashti A, Adlan MN, Abdul Aziz H, Ibrahim AH (2018) Application of response surface methodology (RSM) for optimization of ammoniacal nitrogen removal from palm oil mill wastewater using limestone roughing filter. J Appl Res Water Wastewater 5(1):411–416. https://doi.org/10.22126/arww.2018.892

Foo KY, Hameed BH (2012) Microwave-assisted preparation and adsorption performance of activated carbon from biodiesel industry solid reside: influence of operational parameters. Bioresour Technol 103(1):398–404. https://doi.org/10.1016/j.biortech.2011.09.116

Gamoudi S, Srasra E (2019) Adsorption of organic dyes by HDPy+-modified clay: effect of molecular structure on the adsorption. J Mol Struct. https://doi.org/10.1016/j.molstruc.2019.05.055

Ghiyasiyan-Arani M, Salavati-Niasari M, Naseh S (2017) Enhanced photodegradation of dye in waste water using iron vanadate nanocomposite; ultrasound-assisted preparation and characterization. Ultrason Sonochem 39:494–503. https://doi.org/10.1016/j.ultsonch.2017.05.025

Gollakota ARK, Munagapati VS, Volli V, Gautam S, Wen J-C, Shu C-M (2021) Coal bottom ash derived zeolite (SSZ-13) for the sorption of synthetic anion Alizarin Red S (ARS) dye. J Hazard Mater 416:125925. https://doi.org/10.1016/j.jhazmat.2021.125925

Guo S, Zheng F, Xu J, Jiang J, Cui Z, Wu C, Lin Y, Sun Q, Zheng Y, Sa B (2025) Enhanced fluoride removal from drinking water by activated carbon supported Ce–Al oxides: performance and mechanism [10.1039/D5RA00397K]. RSC Adv 15(18):14363–14374. https://doi.org/10.1039/D5RA00397K

Habiba U, Lee JJL, Joo TC, Ang BC, Afifi AM (2019) Degradation of methyl orange and congo red by using chitosan/polyvinyl alcohol/TiO2 electrospun nanofibrous membrane. Int J Biol Macromol 131:821–827. https://doi.org/10.1016/j.ijbiomac.2019.03.132

Igwegbe CA, Ighalo JO, Ghosh S, Ahmadi S, Ugonabo VI (2023) Pistachio (*Pistacia vera*) waste as adsorbent for wastewater treatment: a review. Biomass Convers Biorefin 13(10):8793–8811. https://doi.org/10.1007/s13399-021-01739-9

Islam MT, Saenz-Arana R, Hernandez C, Guinto T, Ahsan MA, Bragg DT, Wang H, Alvarado-Tenorio B, Noveron JC (2018) Conversion of waste tire rubber into a high-capacity adsorbent for the removal of methylene blue, methyl orange, and tetracycline from water. J Environ Chem Eng 6(2):3070–3082. https://doi.org/10.1016/j.jece.2018.04.058

Jiang Y, Liu B, Xu J, Pan K, Hou H, Hu J, Yang J (2018) Cross-linked chitosan/β-cyclodextrin composite for selective removal of methyl orange: adsorption performance and mechanism. Carbohydr Polym 182:106–114. https://doi.org/10.1016/j.carbpol.2017.10.097

Karimi Anjiraki M, Ghiyasiyan-Arani M, Falah Khudair Z, Baladi M, Shabani-Nooshabadi M, Salavati-Niasari M (2024) A highly efficient PrMnO3/graphene oxide nanocomposite for visible light induced photocatalytic water treatment. Solar Energy 275:112615. https://doi.org/10.1016/j.solener.2024.112615

Khan AA, Molla A, Chowdhury A, Kumari S, Hussain S (2021) Surface-charge-controlled synthesis of ZnIn2S4 nanosheet-based materials for selective adsorption of organic dyes. ACS Appl Nano Mater 4(4):4114–4128. https://doi.org/10.1021/acsanm.1c00409

Krishna LS, Soontarapa K, Asmel NK, Kabir MA, Yuzir A, Zuhairi WYW, Sarala Y (2019) Adsorption of acid blue 25 from aqueous solution using zeolite and surfactant modified zeolite. Desalination Water Treat 150:348–360. https://doi.org/10.5004/dwt.2019.23726

Kumar MS, Selvam V, Vadivel M (2012) Synthesis and characterization of silane modified iron (III) oxide nanoparticles reinforced chitosan nanocomposites. Eng Sci Adv Technol 2:1258–1263

Lakkaboyana SK, Soontarapa K, Asmel NK, Kumar V, Marella RK, Yuzir A, Wan Yaacob WZ (2021) Synthesis and characterization of Cu(OH)2-NWs-PVA-AC nano-composite and its use as an efficient adsorbent for removal of methylene blue. Sci Rep 11(1):5686. https://doi.org/10.1038/s41598-021-84797-3

Li Q, Zhang L, Zhang L, Wu X (2021) Optimizing energy efficiency and thermal comfort in building green retrofit. Energy 237:121509. https://doi.org/10.1016/j.energy.2021.121509

Losetty V, Devanesan S, AlSalhi MS, Velu PP, Muthupillai D, Kumar KA, Lakkaboyana SK (2024) Green synthesis of silver nanoparticles using *Malachra alceifolia* (wild okra) for wastewater treatment and biomedical applications with molecular docking approach. Environ Sci Pollut Res 31(43):55562–55576. https://doi.org/10.1007/s11356-024-34872-9

Ma P, Geng Q, Gao X, Yang S, Liu G (2016) Solution combustion of spinel CuMn2O4 ceramic pigments for thickness sensitive spectrally selective (TSSS) paint coatings. Ceram Int 42(10):11966–11973. https://doi.org/10.1016/j.ceramint.2016.04.122

Madrakian T, Abbas A, Rezvani JN, Ahmadi M (2013) Kinetic and thermodynamic studies of the adsorption of several anionic dyes from water samples on magnetite-modified multi-walled carbon nanotubes. Sep Sci Technol 48(17):2638–2648. https://doi.org/10.1080/01496395.2013.805419

Masoumi H, Ghaemi A, Ghanadzadeh Gilani H (2021) Exploiting the performance of hyper-cross-linked polystyrene for removal of multi-component heavy metal ions from wastewaters. J Environ Chem Eng 9(4):105724. https://doi.org/10.1016/j.jece.2021.105724

Mobarak M, Selim AQ, Mohamed EA, Seliem MK (2018) A superior adsorbent of CTAB/H_2O_2 solution–modified organic carbon rich-clay for hexavalent chromium and methyl orange uptake from solutions. J Mol Liq 259:384–397. https://doi.org/10.1016/j.molliq.2018.02.014

Mohassel R, Sobhani A, Salavati-Niasari M, Goudarzi M (2018) Pechini synthesis and characteristics of Gd_2CoMnO_6 nanostructures and

its structural, optical and photocatalytic properties. Spectrochim Acta A Mol Biomol Spectrosc 204:232–240. https://doi.org/10.1016/j.saa.2018.06.050

Monsef R, Soofivand F, Abbas Alshamsi H, Al-Nayili A, Ghiyasiyan-Arani M, Salavati-Niasari M (2021) Sonochemical synthesis and characterization of $PrVO_4$/CdO nanocomposite and their application as photocatalysts for removal of organic dyes in water. J Mol Liq 336:116339. https://doi.org/10.1016/j.molliq.2021.116339

Mousavi-Kamazani M (2019) Facile hydrothermal synthesis of egg-like $BiVO_4$ nanostructures for photocatalytic desulfurization of thiophene under visible light irradiation. J Mater Sci Mater Electron 30(19):17735–17740. https://doi.org/10.1007/s10854-019-02123-0

Phan TTV, Phan DT, Cao XT, Huynh TC, Oh J (2021) Roles of chitosan in green synthesis of metal nanoparticles for biomedical applications. Nanomaterials (Basel). https://doi.org/10.3390/nano11020273

Pramothkumar A, Senthilkumar N, Jothivenkatachalam K, Fermi Hilbert Inbaraj P (2019) Flake-like CuMn2O4 nanoparticles synthesized via co-precipitation method for photocatalytic activity. Phys B: Condens Matter 572:117–124. https://doi.org/10.1016/j.physb.2019.07.047

Rahmatolahzadeh R, Mousavi-Kamazani M, Shobeiri SA (2017) Facile co-precipitation-calcination synthesis of $CuCo_2O_4$ nanostructures using novel precursors for degradation of Azo Dyes. J Inorg Organomet Polym Mater 27(1):313–322. https://doi.org/10.1007/s10904-016-0473-9

Rohokale MS, Dhabliya D, Sathish T, Vijayan V, Senthilkumar N (2021) A novel two-step co-precipitation approach of CuS/$NiMn_2O_4$ heterostructured nanocatalyst for enhanced visible light driven photocatalytic activity via efficient photo-induced charge separation properties. Phys B Condens Matter 610:412902. https://doi.org/10.1016/j.physb.2021.412902

Samadi Kazemi M, Sobhani A (2023) CuMn2O4/chitosan micro/nanocomposite: green synthesis, methylene blue removal, and study of kinetic adsorption, adsorption isotherm experiments, mechanism and adsorbent capacity. Arab J Chem 16(6):104754. https://doi.org/10.1016/j.arabjc.2023.104754

Sedighi F, Sobhani-Nasab A, Behpour M, Rahimi-Nasrabadi M (2019) Photocatalytic degradation of rhodamine B, and phenol red dyes using NiMn2O4 nanoparticles prepared by a new approach. J Nanostruct 9(2):258–267. https://doi.org/10.22052/JNS.2019.02.008

Sharma M, Sharma R (2020) Zn-ion batteries: ZnMn2O4 as cathode material. Mater Today Proc 26:3378–3385. https://doi.org/10.1016/j.matpr.2019.10.152

sobhani A (2022) Mn/Cu/O/ Chitosan Nanocomposites: hydrothermal synthesis, characterization, and its application for adsorptive removal of methylene blue from wastewater. J Nanostruct 12(3):746–753. https://doi.org/10.22052/JNS.2022.03.027

Sobhani A (2024) Ni/MnO/chitosan nanocomposites: synthesis, characterization and investigation of photocatalytic applications for degradation of malachite green. J Mater Sci: Mater Electron 35(9):673. https://doi.org/10.1007/s10854-024-12456-0

Sobhani A, Salavati-Niasari M (2015) CdSe nanoparticles: facile hydrothermal synthesis, characterization and optical properties. J Mater Sci: Mater Electron 26(9):6831–6836. https://doi.org/10.1007/s10854-015-3297-4

Thamer BM, Shaker AA, Hameed A, M. M., Al-Enizi AM (2023) Highly selective and reusable nanoadsorbent based on expansive clay-incorporated polymeric nanofibers for cationic dye adsorption in single and binary systems. J Water Process Eng 54:103918. https://doi.org/10.1016/j.jwpe.2023.103918

Wang LJ, Zhou Q, Liang Y, Shi H, Zhang G, Wang B, Zhang W, Lei B, Wang WZ (2013) Size effect and enhanced photocatalytic activity of CuO sheet-like nanostructures prepared by a room temperature solution phase chemical method. Appl Surf Sci 271:136–140. https://doi.org/10.1016/j.apsusc.2013.01.148

Wang Y, He L, Li Y, Jing L, Wang J, Li X (2020) Ag NPs supported on the magnetic Al-MOF/PDA as nanocatalyst for the removal of organic pollutants in water. J Alloys Compd 828:154340. https://doi.org/10.1016/j.jallcom.2020.154340

Wang K, Song Z, Xu Z, Xi Y, Cui Y, Zhou H (2025) Synthesis of quaternized magnetic chitosan and adsorption performance for methyl orange from aqueous solution††Electronic supplementary information (ESI) available. RSC Adv 15(26):21121–21132

XinxinYang, Li Y, Gao H, Wang C, Zhang X, Zhou H (2018) One-step fabrication of chitosan-Fe(OH)3 beads for efficient adsorption of anionic dyes. Int J Biol Macromol 117:30–41. https://doi.org/10.1016/j.ijbiomac.2018.05.137

Yu J, Zhang X, Wang D, Li P (2018) Adsorption of methyl orange dye onto biochar adsorbent prepared from chicken manure. Water Sci Technol 77(5–6):1303–1312. https://doi.org/10.2166/wst.2018.003

Zhang Y-R, Wang S-Q, Shen S-L, Zhao B-X (2013) A novel water treatment magnetic nanomaterial for removal of anionic and cationic dyes under severe condition. Chem Eng J 233:258–264. https://doi.org/10.1016/j.cej.2013.07.009

Zhang L, Qian L, Pan H,and, Huang R (2016) Adsorptive removal of methyl orange using enhanced cross-linked chitosan/bentonite composite. Desalination Water Treat 57(36):17011–17022. https://doi.org/10.1080/19443994.2015.1088478

Zhang B, Yunhai W,and, Cha L (2020) Removal of methyl orange dye using activated biochar derived from pomelo peel wastes: performance, isotherm, and kinetic studies. J Dispers Sci Technol 41(1):125–136. https://doi.org/10.1080/01932691.2018.1561298

Zhang C, Xie A, Zhang W, Chang J, Liu C, Gu L, Duo X, Pan F, Luo S (2021) CuMn2O4 spinel anchored on graphene nanosheets as a novel electrode material for supercapacitor. J Energy Storage 34:102181. https://doi.org/10.1016/j.est.2020.102181

Zinatloo-Ajabshir S, Salavati-Niasari M (2019) Preparation of magnetically retrievable CoFe2O4@SiO2@Dy2Ce2O7 nanocomposites as novel photocatalyst for highly efficient degradation of organic contaminants. Compos Part B-Eng 174:106930. https://doi.org/10.1016/j.compositesb.2019.106930

Zinatloo-Ajabshir S, Morassaei MS, Salavati-Niasari M (2019) Eco-friendly synthesis of Nd2Sn2O7–based nanostructure materials using grape juice as green fuel as photocatalyst for the degradation of erythrosine. Compos Part B Eng. https://doi.org/10.1016/j.compositesb.2019.03.045

Zinatloo-Ajabshir S, Morassaei MS, Amiri O, Salavati-Niasari M (2020a) Green synthesis of dysprosium stannate nanoparticles using *Ficus carica* extract as photocatalyst for the degradation of organic pollutants under visible irradiation. Ceram Int 46(5):6095–6107. https://doi.org/10.1016/j.ceramint.2019.11.072

Zinatloo-Ajabshir S, Morassaei MS, Amiri O, Salavati-Niasari M, Foong LK (2020) Nd2Sn2O7 nanostructures: green synthesis and characterization using date palm extract, a potential electrochemical hydrogen storage material. Ceram Int 46(11, Part A):17186–17196. https://doi.org/10.1016/j.ceramint.2020.03.014

Publisher's Note Springer Nature remains neutral with regard to jurisdictional claims in published maps and institutional affiliations.